15

Modeling of Elastic Robot Joints with Nonlinear Damping and Hysteresis

Michael Ruderman
Institute of Control Theory and Systems Engineering, TU-Dortmund
Germany

1. Introduction

Elastic robot joints gain in importance since the nowadays robotics tends to the lightweight structures. The lightweight metals and composite materials deployed not only in the links but also in the joint assemblies affect the overall stiffness of robotic system. The elastic joints provide the loaded robot motion with additional compliance and can lead to significant control errors and vibrations in the joint as well as operational space. A better understanding of the compliant joint behavior can help not only to analyze and simulate robotic systems but also to improve their control performance.
Elastic robot joints are often denoted as flexible joints or compliant joints as well. The former modeling approaches aimed to describe the dynamic behavior of elastic robot joints lead back to Spong (1987). Spong extended the general motion equation of a rigid robotic manipulator to the case of joint elasticity captured by a linear connecting spring. Remember that the general motion equation derived either from Lagrange or Newton-Euler formalism for a class of rigid robotic manipulators (Sciavicco & Siciliano (2000)) can be expressed as

$$\mathbf{M}(\mathbf{q})\ddot{\mathbf{q}} + \mathbf{C}(\mathbf{q}, \dot{\mathbf{q}})\dot{\mathbf{q}} + \mathbf{G}(\mathbf{q}) = \mathbf{u}\,. \tag{1}$$

Here, $\mathbf{q} \in \mathbb{R}^n$ is the vector of Lagrangian (also joint) coordinates and $\mathbf{u} \in \mathbb{R}^n$ is the vector of generalized input forces. The configuration dependent matrixes $\mathbf{M} \in \mathbb{R}^{n\times n}$, $\mathbf{C} \in \mathbb{R}^{n\times n}$, and $\mathbf{G} \in \mathbb{R}^n$ constitute the inertia, Coriolis-centrifugal, and gravity terms correspondingly. The model introduced by Spong (1987) has been widely used in the later works which deal with a compliance control (Zollo et al. (2005)) and passivity-based impedance control (Ott et al. (2008)) of robots with joint elasticities. Despite a good acceptance for the control applications this modeling strategy misses the damping factor related to the connecting spring. In this regard, the approach proposed by Ferretti et al. (2004) which provides two masses connected by a linear spring and damper arranged in parallel is more consistent with the physical joint structure. Also the inverse dynamic model used for vibration control of elastic joint robots (Thummel et al. (2005)) incorporates a torsional spring with both stiffness and damping characteristics. From a slightly diversing point of view the modeling of elastic robot joints was significantly influenced by the studies of harmonic drive gear transmission performed in the end-nineties and last decade. The harmonic drives are widely spread in the robotic systems due to their compact size, high reduction ratios, high torque capacity, and low (nearly zero) backlash. However, a specific mechanical assembly

provides the harmonic drive gears with additional elasticities which are strongly coupled with frictional effects. A structure-oriented dissipative model of the harmonic drive torque transmission was proposed by Taghirad & Bélanger (1998). The model composes multiple component-related frictional elements and an additional structural damping attributed to the flexspline. Another notable modeling issue provided by Dhaouadi et al. (2003) presents the torsional torque in harmonic drives as an integro-differential hysteresis function of both angular displacement and angular velocity across the flexspline. Later, Tjahjowidodo et al. (2006) describe the dynamics in harmonic drives using nonlinear stiffness characteristics combined with distributed Maxwell-slip elements that capture the hysteresis behavior. A complex phenomenological model of elastic robot joints with coupled hysteresis, friction and backlash nonlinearities was proposed by Ruderman et al. (2009). However, realizing the complexity of decomposing and identifying the single nonlinearities a simplified nonlinear dynamic model was later introduced in Ruderman et al. (2010).

The leitmotif provided in this Chapter is to incorporate a combined physical as well as phenomenological view when modeling the joint transmission with elasticities. Unlike the classical approaches which rather operate with linear stiffness and damping elements arranged either in series or in parallel the structure-oriented effects are emphasized here. The inherently nonlinear compliance and damping of elastic robot joints are tackled from the cause-and-effect point of view. It is important to note that such approaches can rapidly increase the number of free parameters to be identified, so that the model complexity has to be guarded carefully. The Chapter is organized as follows. Section 2 introduces the robot joint topology which captures equally the dynamic behavior of both rigid and elastic revolute joints. Three closed subsystems are described in terms of their eigenbehavior and feedforward and feedback interactions within the overall joint structure. Section 3 provides the reader with description of the developed joint model capable to capture two main nonlinearities acting in the joint transmission. First, the dynamic joint friction is addressed. Secondly, the nonlinear stiffness combined with hysteresis map is described in detail. An experimental case study provided in Section 4 shows some characteristical observations obtained on a laboratory setup of the joint with elasticities and gives some identification results in this relation. The main conclusions are derived in Section 5.

2. Robot joint topology

Before analyzing the dynamic behavior of an elastic robot joint an underlying joint topology has to be assumed first. Different topologies of robotic joints are conceivable starting from the more simple linear structures as used e.g. by Ferretti et al. (2004), Zollo et al. (2005), Albu-Schaffer et al. (2008) and migrating towards the more complex nonlinear approaches as proposed e.g. by Taghirad & Bélanger (1998), Dhaouadi et al. (2003), Tjahjowidodo et al. (2006), particularly in context of harmonic drive gear transmissions. Here it is important at which level of detail the robot joint transmission could be described. Mostly it is conditioned by the available knowledge about the mechanical joint structure and the accessibility of system measurements required for the identification. In majority of applications, the actuator measurements such as the angular position and velocity as well as active motor current are available only prior to the gear transmission. In more advanced but also more cost-intensive applications like DLR lightweight robots (see e.g. by Albu-Schaffer et al. (2008)), the angular motion and torque measurements are available at both actuator and load side of the

joint transmission. Although those hardware solutions are often not technically or (and) economically profitable, a prototypic laboratory measurement performed on the load side of robotic joints can yield adequate data sufficient for analysis and identification. Here, one can think about highly accurate static as well as dynamic measurements of the joint output position performed by means of the laser interferometry or laser triangulation. The load torques can also be determined externally either by applying an appropriate accelerometer or by using locked-load mechanisms equipped by the torque (load) cells. However, the latter solution is restricted to the quasi-static experiments with a constrained output motion.
Now let us consider the topology of an elastic robot joint as shown in Fig. 1. In terms of the input-output behavior the proposed structure does not substantially differ from a simple fourth-order linear dynamic model of two connected masses. An external exciting torque u constitutes the input value and the relative position of the second moving mass θ constitutes the output value we are interested in. Going into the input-output representation,

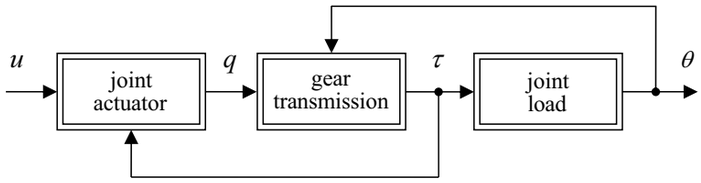

Fig. 1. Topology of elastic robot joint

let us subdivide the robotic joint into three close subsystems connected by the feedforward and feedback actions realized by appropriate physical states. The joint actuator loaded by the feedback torque τ provides the output angular displacement q of a rigid shaft. This value is an inherent determinant of the relative motion entering the gear transmission and mostly measurable prior to that one. Since the gear transmission captures the intrinsic joint elasticity, the angular output displacement of the joint load constitutes the second feedback state. Assuming that the gear with elasticities behaves like a torsion spring with a certain stiffness capacity its output value represents the transmitted torque which drives the joint load. When cutting free the forward and feedback paths the joint model decomposes into three stand-alone submodels, each one describing the specified physical subsystem. Note that from energy conversion point of view we obtain three dissipative mappings with two different sets of the input values. The first input set constitutes the forward propagation of the energy fed to the system. The second input set represents the system reaction with a negative or positive energy feedback depending on the instantaneous operation state. The superposition of the feed-in and reactive joint torque provides the internal angular motion $(u - \tau) \mapsto q$ damped by the friction. The constrained relative displacement across the gear transmission provides the elastic tension in the joint $(q - \theta) \mapsto \tau$ damped by its structure. Finally, the transmitted torque provides the output relative motion $\tau \mapsto \theta$ whose damping depends on the topology of subsequent load.
The actual joint topology represents a general case which covers both elastic and rigid transmission. The actuator submodel can be equally used for a rigid joint modeling, where τ will appear as an input disturbance fed back directly from the joint load and acting upon the overall torque balance. The stand-alone gear transmission modeling is however meaningful only when the relative displacement occurs, i.e. $q \neq \theta$. When considering a rigid robotic joint

the transmission submodel will describe a particular case with an unlimited stiffness. At this, each infinitesimal change in q will lead to an immediate excitation of the load part, so that the eigendynamics of the joint transmission disappears.
The following analytical example of two equivalent linear joint models explains the upper mentioned ideas in more detail. For instant, consider a simple motion problem of two connected masses m and M with two damping factors d and D, once with a rigid and once with an elastic joint. Assume that the last one is represented by the spring with the stiffness K. The first case can be described by the simple differential equation

$$(m+M)\,\ddot{q} + (d+D)\,\dot{q} = u\,. \tag{2}$$

It is evident that the system (2) provides the single dynamic state, and the mass and damping factors appear conjointly whereas $q = \theta$. The more sophisticated second case with elasticity requires two differential equations

$$\begin{aligned} m\,\ddot{q} + d\,\dot{q} + K(q-\theta) &= u\,, \\ M\,\ddot{\theta} + D\,\dot{\theta} - K(q-\theta) &= 0 \end{aligned} \tag{3}$$

which constitute the fourth-order dynamic system. For both systems, let us analyze the step response in time domain and the amplitude response in frequency domain shown in Fig. 2 (a) and (b). Here, $\mathrm{H}_1(s)$ denotes the transfer function $\mathrm{H}(s) = \dot{\theta}(s)/U(s)$ of Eq. (2), and $\mathrm{H}_2(s)$ as well as $\mathrm{H}_3(s)$ denote the one of Eq. (3). At this, the stiffness K is set to 1e3 for $\mathrm{H}_2(s)$, and to 1e8 for $\mathrm{H}_3(s)$. The case described by $\mathrm{H}_3(s)$ should approximate a rigid system at which the stiffness increases towards unlimited. Note that the residual parameters of Eqs. (2) and (3) remain constant. It is easy to recognize that the step response of $\mathrm{H}_3(s)$ coincides well with those one of the absolute rigid joint $\mathrm{H}_1(s)$. When analyzing the frequency response function it can be seen that the resonance peak of $\mathrm{H}_3(s)$ is shifted far to the right comparing to $\mathrm{H}_2(s)$. Up to the resonance range the frequency response function $\mathrm{H}_3(s)$ coincides exactly with $\mathrm{H}_1(s)$. Note that the shifted resonance of $\mathrm{H}_3(s)$ provides the same peak value as $\mathrm{H}_2(s)$. Hence, during an exceptional excitation exactly at the resonance frequency the oscillatory output will arise again. However, from the practical point of view such a high-frequently excitation appears as hardly realizable in a mechanical system. Even so, when approaching the resonance range, the high decrease of the frequency response function provides a high damping within the overall system response.

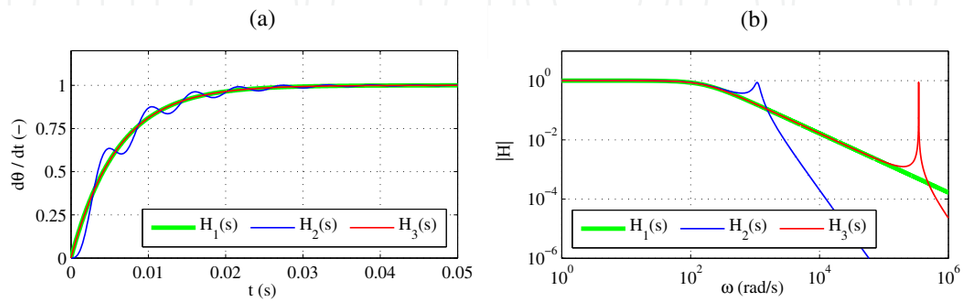

Fig. 2. Comparison of linear joint approaches; step response (a), frequency response (b)

The performed qualitative example demonstrates the universal character of the proposed joint topology. At this, the principal mechanisms conducting the joint dynamics are independent

from the complexity of a particular robotic system. Being conditional upon the gear and bearing structure an optimal level of detail for modeling can be determined using a top-down approach. Starting from the simplest rigid case with a single actuator damping, additional compliant and frictional elements can be included hierarchically in order to particularize the case-specific system behavior.
In the following, we consider the single modeling steps required to achieve an adequate description of each subsystem included in the topology of a nonlinear elastic joint.

2.1 Joint actuator

Considering the joint actuator which is driven by an electrical servo motor the angular velocity and angular position of the output shaft are determined by two input values. The first one is the input torque u which induces the angular acceleration of the rotor. The second one is a feedback load torque τ which antagonizes the controllable motion and thus behaves as a disturbance value to be accounted for. The conjoint moment of inertia m includes the rotor with shaft as well as the additional rotating elements such as encoders, breaks, and couplings. Mostly, it can be supposed that all rotating bodies are homogenous and axially symmetrical. This straightforward simplification allows us to deal with the concentrated model parameters and to consider the relative motion at this stage as the single body dynamics. The joint actuator can be described as follows

$$m\,\ddot{q} + f(\dot{q}) + \tau = u\,, \tag{4}$$

in which the input torque is assumed to be linear to the regulated motor current i. The fast current controls of the common servo motors operate at sampling rates about or larger than 10 kHz. Hence, the transient behavior of the current control loop can be easily neglected taking into account the time constants of the mechanical system part. The latter amount to several tens up to some hundred milliseconds. With an appropriate current regulation an electrical servo motor can be considered as a nearly reactionless power source which provides the joint actuator with the driving input torque $u(t) \cong k_m i(t)$.
The friction $f(\cdot)$ acting in the bearings is in large part load-independent. However, since a particular joint actuator can be mounted on the robotic manipulator with multiple degrees of freedom (DOF) its frictional characteristics can vary dependent on the actual robot configuration. Particularly, the orientation of the supported motor shaft to the gravity field can influence the breakaway and sliding friction properties to a certain degree. Aside of the dependency from the robotic configuration the most significant frictional variations, as well known, are due to the thermal effects. Both the external environment temperature and the internal temperature of contacting elements play a decisive role, whereas the last one increases usually with the operating time and intensity. However, the thermal frictional effects can be rather attributed to a slow time-variant process and a corresponding adaptivity of the model parameters. For reason of clarity an explicit temperature dependency is omitted here just as in most known approaches of modeling the robot dynamics. In the following, we also assume that no significant eccentricities are present in the system, so that almost no periodic torque ripples occur on a shaft revolution. Otherwise, the harmonic disturbances partially attributed to the position-dependent friction can be efficiently estimated and compensated as proposed e.g. by De Wit & Praly (2000).
The complexity of the obtained actuator model can differ in number of the free parameters to be identified, mostly dependent on the selected mapping of the friction behavior. The lumped

moment of inertia can be easily estimated by decoupled load using the large steps and (or) free run-out experiments. However, in doing so a linear damping has to be assumed. Since the motion is essentially damped by a nonlinear friction it appears as more reasonable to identify the actuator inertia together with the corresponding friction parameters. For these purposes more elaborated and specially designed experiments either in time or frequency domain can be required (see e.g. by Ruderman & Bertram (2011a)). Often, it is advantageous to identify the actuator friction together with the friction acting in the gear transmission. The friction effects in the actuator and gear assembly are strongly coupled with each other since no significant elasticities appear between both. When identifying the dynamic friction one has to keep in mind that the captured torque value, mostly computed from the measured motor current, represents a persistent interplay between the system inertia and frictional damping.

2.2 Gear transmission

The mechanical gear transmission can be considered as a passive transducer of the actuator motion to the output torque which drives the joint load. At this, the angular position of the joint load constitutes the feedback value which contains the signature of elasticities and backlash acting in the transmission system. Often, the gear transmission provides the main source of nonlinearities when analyzing the joint behavior, the reason for which several applications arrange the direct drives without gear reduction (see e.g. by Ruderman et al. (2010)). However, most nowadays robotic systems operate using the gear units which offer the transmission ratios from 30:1 up to 300:1. Apart from the classical spur gears the more technologically elaborated planetary and harmonic drive gears have been established in robotics for several years. Different gear types exhibit quite differing level of torsional compliance and mechanical play, also known as backlash.

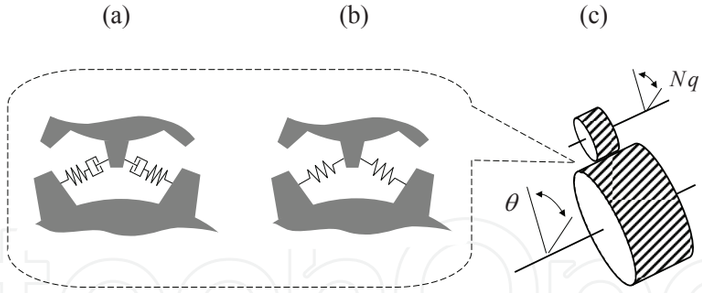

Fig. 3. Gear transmission with elasticities and backlash

An idealized rigid gear with a transmission ratio N provides the angular motion reduction

$$\theta = \frac{1}{N} q \tag{5}$$

and the corresponding torque gain

$$T = N \tau \,. \tag{6}$$

Due to the gear teeth meshing the disturbing torsional compliance and backlash can occur during a loaded motion. Assuming the rotationally symmetrical gear mechanisms, i.e. excluding any rotary cam structures, the cumulative effects of the gear teeth meshing can be

represented as shown schematically in Fig. 3. Here in (a), the angular relative displacement

$$\delta = N\,q - \theta \tag{7}$$

is additionally subject to a backlash. However, the latter one can be neglected when the play size stays below the resolution of q and θ measurement. Thereafter, the case (b) represents a pure elastic deflection of the teeth meshing, whereat the corresponding compliance is not mandatory linear. In fact, it is rather expected that the teeth interaction exhibits a hardening stiffness property. Due to internal frictional mechanisms within the teeth engagement area the overall torsional joint compliance can behave piecewise as elasto-plastic and thus give rise to substantial hysteresis effects. The backlash, even when marginal, is coupled with an internal teeth friction and thus provides a damped bedstop motion. Due to a mutual interaction between the mentioned nonlinear phenomena the resulting hysteresis is hardly decomposable in proper frictional, structural and backlash elements. Hence, it must be rather considered as a compound input-output nonlinearity, while keeping in mind the nature of its internal mechanisms.

The overall hysteresis torque can be considered as a general nonlinear function

$$T(t) = h\big(\delta(t),\, \delta(0)\big) \tag{8}$$

of the relative displacement, and that under impact of the initial condition $\delta(0)$. The latter is poorly known when the absolute angular position is captured neither on the input nor output side of the joint, that is the most typical case in the robotic praxis. In this regard, it could be necessary first to saturate the transmission load in order to determine a proper hysteresis state which offers a well known memory effect. Here, the hysteresis memory manifests itself in the transmitted torque value which depends not only on the recent relative displacement between the gear input and output but equally on the history of the previous values. Thus, the dynamic hysteresis map has to replace the static stiffness characteristic curve of the gear transmission. However, the last one remains a still suitable approximation sufficient for numerous practical applications. Well understood, the hysteretic torque transmission includes an inherent damping which is characterized by the energy dissipation on a closed load-release cycle. The enclosed hysteresis loop area provides a measure of the corresponding structural losses, where the damping ratio is both amplitude- an frequency-dependent. Thus, the structural hysteresis damping differs from the linear viscous one and can lead to the limit cycles and multiple equilibrium states.

The following numerical example demonstrates the damping characteristics of the joint transmission in a more illustrative way. For instance, the single mass with one DOF is connected to the ground, once using a linear spring with linear viscous damping, and once using a nonlinear hysteretic spring. At this, the linear stiffness is selected so as to coincide with the average value of the nonlinear stiffness map included in the hysteresis model. When exciting the system by the Dirac impulse (at time t=1) the eigenmotion behaves as a damped oscillation shown in Fig. 4. The linear case (a) provides a typical second-order oscillatory response which is dying out towards zero equilibrium state, having an exponential enveloping function. In case (b), the nonlinear hysteretic spring is higher damped at the beginning, though does not provide a final equilibrium state. Instead of that, the motion enters a stable limit cycle up from a certain amplitude. The last one indicates the hysteresis cancelation close to zero displacement that is however case-specific and can vary dependent

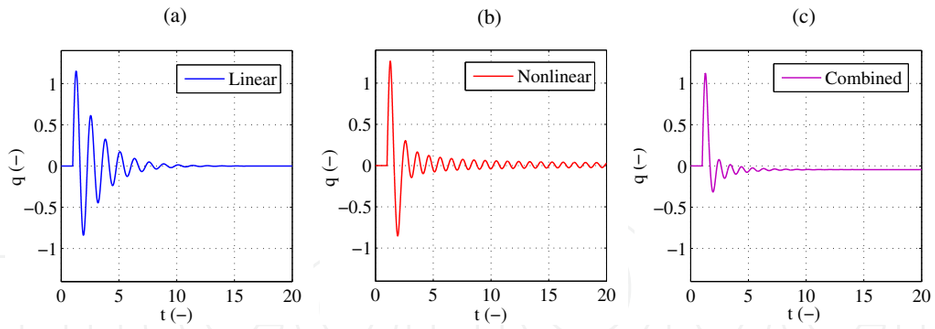

Fig. 4. Damped response of the excited eigenmotion when applying linear and nonlinear hysteretic spring

on the selected hysteresis map. From a physical point of view an autonomous mechanical system will surely converge to a static idle state due to additional damping mechanisms not necessarily captured by the hysteresis. However, theoretically seen the hysteresis damping does not guarantee the full decay of all eigenmotions. An interesting and more realistic case (c) represents a combination of the linear and nonlinear hysteretic damping. Due to an additional velocity-dependent damping term the eigenmotion does not stay inside of a limit cycle and converges towards a non-zero idle state, thus providing the system response with memory. The characteristical nonzero equilibrium states denote the forces remaining in the gear transmission after the input and output loads drop out.

2.3 Joint load

The robot links which connect the single joints within the kinematic chain of manipulator constitute the moving bodies with additional inertia and elasticities. They may generate lightly damped vibrational modes, which reduce the robot accuracy in tracking tasks according to Zollo et al. (2005).

The overall multi-body manipulator dynamics (1) provides the interaction between the actuated joints and passive links. Recall that Eq. (1) captures a rigid robot structure with no elasticities at all. However in general case, the contribution of the gravity and Coriolis-centrifugal forces has to be taken into account independent of the considered rigid or elastic manipulator. For reason of traceability, we cut free the kinematic chain and consider the single robot joint with the following link as depicted in Fig. 5. At this, the joint link can be represented either as the concentrated L or distributed $L_1, \ldots, L_n$ mass. Here, no additional inertia and Coriolis-centrifugal terms fed back from the following joints and links contribute to the overall load balance. Note that the recent approach constitutes a strong simplification of the link dynamics so that the additional degree of freedom $\theta_L = \theta - \alpha$ or $\theta_L = \theta - \sum \alpha_i$ for case (b) is used to capture the vibrational disturbances only. It means that in terms of the distributed impact of gravity the angular link deflection α is assumed to be small enough, so that $\sin(\theta) \approx \sin(\theta - \alpha)$ and

$$G = l\, \mathrm{g}\, \sin(\theta)\,. \tag{9}$$

Here, g denotes the gravity constant and l is the lever of COG (center of gravity). The transmitted torque τ drives the joint output with inertia M and bearing friction which can be captured in a simplified way using Coulomb and viscous friction $F_c\, \mathrm{sgn}(\dot{\theta}) + d_f\, \dot{\theta}$ only.

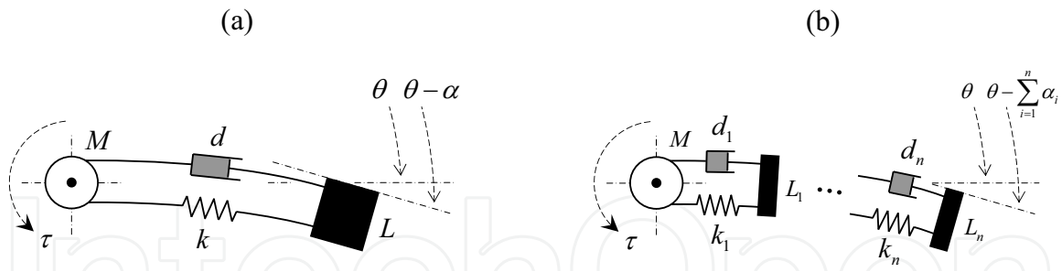

Fig. 5. Concentrated (a) and distributed (b) joint load

For reasons of clarity let us analyze here the case of a concentrated mass shown in Fig. 5 (a). At this point it is important to say that the load model with distributed masses shown in Fig. 5 (b) can behave more accurately and capture more complex vibration modes. At the same time, the identification of distributed mass-stiffness-damper parameters can rapidly exceed the given technical conditions of the system measurement. Besides, the achieved gain in accuracy of capturing the reactive load related to vibrations is not necessarily high. Recall that the primary objective here is to determine the reactive torque fed back from the oscillating elastic link and thus to improve the prediction of θ. An accurate computation of the link end-position due to link elasticities is surely also an important task in robotics. However, this falls beyond the scope of the current work whose aim is to describe the robot joint transmission with nonlinearities. Introducing the state vector $\mathbf{x} = (\theta\ \dot{\theta}\ \theta_L\ \dot{\theta}_L)^T$ and the vector of nonlinearities $\mathbf{h} = \left(\sin(\theta)\ \mathrm{sgn}(\dot{\theta})\ 0\ 0\right)^T$ one can obtain the state-space model of the concentrated joint load given by

$$\dot{\mathbf{x}} = \begin{pmatrix} 0 & 1 & 0 & 0 \\ -k/M & -(d_f+d)/M & k/M & d/M \\ 0 & 0 & 0 & 1 \\ k/L & d/L & -k/L & -d/L \end{pmatrix} \mathbf{x} + \begin{pmatrix} 0 & 0 & 0 & 0 \\ -lg/M & -F_c/M & 0 & 0 \\ 0 & 0 & 0 & 0 \\ 0 & 0 & 0 & 0 \end{pmatrix} \mathbf{h} + \begin{pmatrix} 0 \\ N/M \\ 0 \\ 0 \end{pmatrix} \tau\,. \tag{10}$$

The 4×4 matrices in Eq. (10) constitute the system matrix of a linear part and the coupling matrix of nonlinearities correspondingly. For all physically reasonable parameter values the system proves to be controllable whereas the input torque τ occurs as always lagged due to preceding dynamics of the joint actuator and gear transmission.

The following numerical example demonstrates the disturbing link vibrations during the torque step whose unavoidable lag is approximated by a first-order low pass filter with cut-off frequency 1000 rad/s. The parameter values are selected so as to provide the relation between both inertia $M/L = 0.1$ and damping $d_f/d = 10000$. Further, two relative stiffness values $1k$ and $10k$ are considered. Since the gravity term is not directly involved into vibrational characteristics it can be omitted at this stage. In the same manner the Coulomb friction nonlinearity which constitutes a constant torque disturbance during an unidirectional motion is also excluded from the computation. The response of the simulated, insofar linear, joint load is shown in Fig. 6. Two stiffness values differing in order of magnitude lead to the oscillating link deflection depicted in Fig. 6 (b) and (c). Besides the differing eigenfrequencies the principal shape of the enveloping function appears as quite similar for both stiffness values.

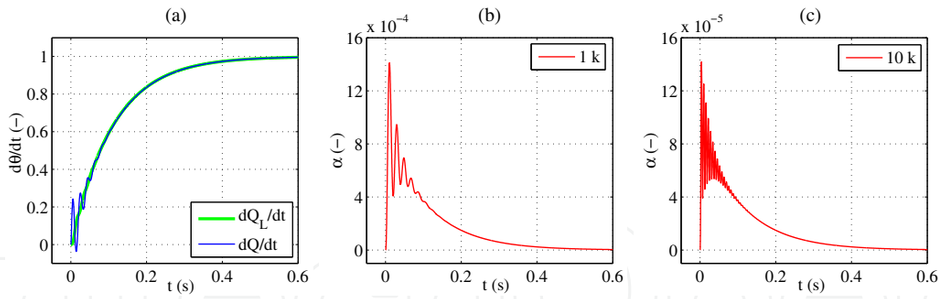

Fig. 6. Response of the joint load with elasticities to the lagged step of the input torque

However, most crucial is the fact that the amplitudes differ in the same order of magnitude, so that a lower stiffness provides a definitely higher level of link vibrations. Considering the correspondent velocity response, once in the joint output and once in the link deflection coordinates depicted in Fig. 6 (a) the impact of the link vibrations becomes evident. Here, the output joint velocity $\dot{\theta}$ is subject to the substantial oscillations at the beginning of relative motion. As a consequence, the oscillating behavior of the joint load will be propagated back to the joint transmission, thus increasing the complexity of overall joint behavior.

3. Nonlinear joint model

The main focus of the current Chapter relates to the grey-box modeling of elastic robot joints with nonlinearities. With respect to the proposed joint topology shown in Fig. 1 that means to derive a particular structure and to find a suitable set of equations to capture the transmission behavior for a class of robotic joints with elasticities. At this, the use of freely parameterizable sub-models and functions allows to describe the system dynamics for different types of gears and bearings involved in the joint assembly. The class of the robot joints aimed to be described here is characterized by a rotary-to-rotary transmission of the actuated relative motion with no position-dependent changes in the joint behavior. That is the input drive torque is transmitted to the joint output by means of the axially symmetric gear mechanisms. Note that the latter, including all bearings and couplings, allow one degree of freedom only. Several types of the gears like harmonic drives, planetary, and diverse subtypes of spur gears fulfill these assumptions, though offering quite differing mechanical principles of the torque transmission.

3.1 Joint structure

The proposed single elastic robot joint with nonlinear damping and hysteresis is shown in Fig. 7. The input drive torque u accelerates the combined actuator mass m, where the friction f constitutes the overall coupled friction of the actuator and gear input. The mechanical joint interface arranges the observation of angular motion, once prior $(q, \dot{q})$ and once beyond $(\theta, \dot{\theta})$ the gear transmission. That is the input and output joint axes are assumed to be rigid outside the employable state measurements. Note that the output joint axis does not necessarily coincide with some physical rotary shaft coming out from the mechanical joint assembly. Just as well it can be a virtual axis of a rotary motion for which the interface will indicate the measuring points. More simply, the input motion interface coincides with the rotary actuator (motor) shaft to which the angular position/velocity measurement is directly applied in the most cases. The nominal gear transmission ratio is denoted by N. The main transmission element with elasticities can be represented by a nonlinear rotary spring with hysteresis Γ.

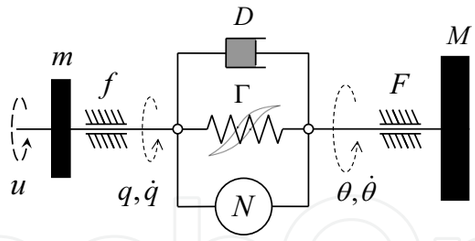

Fig. 7. Elastic robot joint with nonlinear damping and hysteresis

Apart from the hardening stiffness and hysteresis property, the rotary spring can also include the backlash nonlinearities as mentioned afore in Section 2.2. Note that the complexity degree of nonlinearities involved in the transmitting rotary spring can vary. This depends on the required model accuracy as well as significance of each particular phenomenon observable when measuring the joint behavior.

Since the hysteresis map captures the frequency-independent structural damping, an additional linear damping term D is connected in parallel to the rotary spring. The introduced linear damping comprises all viscous (velocity-dependent) dissipative effects arising from the internal teeth and slider interactions as mentioned afore in Section 2.2. Here, one must be aware that the velocity-dependent damping map can ditto possess the nonlinear characteristics. However, for reasons of clarity and more straightforward identification the simple linear damping is further assumed. As shown previously in Fig. 4 (c) the superposition of both damping mechanisms provides the system dynamics with multiple non-zero equilibrium states. Apart from the curvature and area of the underlying hysteresis, which determine the dissipative map, the magnitude of the linear damping affects a faster settling of the oscillatory joint motion.

The moving output joint part is mandatory supported by some rotary-type bearing, so that the output friction torque F has to be included. A proper decomposition of the input and output joint friction appears as one of the most challenging identification tasks when modeling the joint with elasticities. When no sufficient input and output torque measurements are available, certain assumptions about the friction distribution across the joint transmission have to be made. One feasible way to decompose a coupled joint friction is to identify first the overall friction behavior under certain conditions, at which the impact of joint elasticities is either negligible or it constitutes a constant bias term. Here, one can think about the drive experiments under reduced (decoupled) or stationary handled joint load. The steady-state velocity drive experiments can constitute the basis for such an identification procedure. Once the overall joint friction is identified it can be decomposed by introducing the weighting functions and finding the appropriate weighting rates within the overall joint dynamics. However, this heuristic method requires a good prior knowledge about the acting joint elasticities. That is the nonlinear spring and damping models have to be identified afore.

3.2 Dynamic friction

The modeling of dynamic friction is one of the crucial tasks in robotics since the joint friction constitutes not only the stabilizing damping but also can lead to large errors in the control. There is a huge number of works dedicated to modeling and compensating the frictional

effects in robotic joints and machine tools (see Armstrong-Helouvry et al. (1994), Bona & Indri (2005), Al-Bender & Swevers (2008) for overview).

Generally, the existent approaches can be subdivided into static and dynamic mapping of kinetic friction. Note that in terms of kinetics the static friction signifies the friction forces acting during a relative motion at constant or slightly changing velocities and not the sticking forces of stationary bodies. Here, the classical constant Coulomb friction and the linear velocity-dependent viscous friction can be involved to describe the frictional forces between two contacting surfaces which slide upon each other. Moreover, the well-known Stribeck effect can be involved to describe the nonlinear transition between the break-away friction at zero velocity and linear viscous friction in a more accurate way. The most dynamic friction models capture both pre-sliding and sliding regimes of the friction and provide the smooth transition through zero velocity without discontinuities typical for static friction models. The most advanced dynamic friction models are also capable of describing such significant frictional phenomena as position-dependent pre-sliding hysteresis and frictional lag in the transient behavior. An extensive comparative analysis of several dynamic friction models, among Dahl, LuGre, Leuven, and GMS one, can be found in Al-Bender & Swevers (2008) and Armstrong-Helouvry & Chen (2008).

Apart from the pre-sliding frictional mechanisms, the main differences between the static and dynamic friction modeling can be explained when visualized in the velocity-force (w, F) coordinates as shown in Fig. 8. The static friction map provides a discontinuity at zero velocity which can lead to significant observation errors and control problems since the system operates with frequent motion reversals. However, when the steady-state operation modes are predominant the static map can be accurate enough to capture the main frictional phenomena. Further, it is easy to recognize that the closer the relative velocity is to zero the larger is the impact of nonlinear Stribeck effect. The peak value at zero velocity indicates the maximal force, also called break-away, required to bear the system from the sticking to the sliding state of continuous motion. Comparing the Stribeck static map with the dynamic

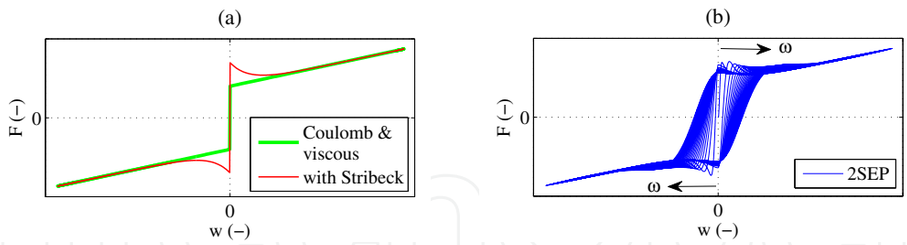

Fig. 8. Static (a) and dynamic (b) friction map in velocity-force coordinates

one shown in Fig. 8 (b) it can be seen that the principal shape of the velocity-force curves remain the same. However, the transient frictional behavior when passing through zero velocity is quite different dependent on the ongoing input frequency ω. Here, the overall friction response to a cyclic input velocity with an increasing frequency is shown. The higher is the ongoing frequency when changing the motion direction the higher is the stretch of the resulting frictional hysteresis. This phenomenon is also known as the frictional lag (see by Al-Bender & Swevers (2008)) since the friction force lags behind the changing relative velocity. Roughly speaking, the frictional lag occurs due to the time required to modify either the hydro-dynamic lubricant properties during the viscous, or the adhesion contact properties during the dry sliding. With an increasing relative velocity after transient response the friction

force is attracted towards the static characteristic curve which represents the steady-state friction behavior. Depicted in Fig. 8 (b), the dynamic friction response is obtained using 2SEP (two-state with elasto-plasticity) model which is briefly described in the rest of this Section.
The 2SEP dynamic friction model (Ruderman & Bertram (2010), Ruderman & Bertram (2011a)) maintains the well-established properties of dynamic friction which can be summarized as i) Stribeck effect at steady-state velocity-dependent sliding, ii) position-dependent pre-sliding hysteresis, and iii) friction lag at transient response. The model describes the dynamic friction behavior using a linear combination of the pre-sliding and transient friction state that converges towards the velocity-dependent steady-state. At this, one independent and one dependent state variables are intuitively related to such frictional phenomena as the pre-sliding hysteresis and friction lag at transient behavior. The weighted superposition of both yields the total friction force as

$$F = A\, z_1 + B\, |w|\, z_2\,. \tag{11}$$

Note that the instantaneous friction value is conducted coevally by the relative displacement and relative velocity without switching functions and (or) thresholds to separate the pre-sliding and sliding regimes. The pre-sliding friction behavior, predominantly captured by z_1, is described using the Modified Maxwell-Slip (MMS) approximation (Ruderman & Bertram (2011b)). The MMS structure can be imagined similar to a single Maxwell-slip element, but with a pivotal difference of representing the applied connecting spring. In MMS model, the irreversible nonlinear spring exhibits a saturating elasto-plastic deflection until a motion reversal occurs. Assuming an exponentially decreasing stiffness by an increasing relative displacement after reversal, the overall hysteretic state converges towards the constant tangential force. It is assumed that the deflection of elasto-plastic asperity contacts saturates at the Coulomb friction level, so that the weighting factor A can be often set to one. A saturated friction state characterizes the plastic sliding at which the deflected asperities slip upon each other and provide an approximately constant value of the tangential force at non-zero velocity. The state dynamic is defined as a first-order nonlinear differential equation

$$\dot{z}_1 = |\Omega|\, w\, K \exp\big(-K|q_r|\big)\,, \tag{12}$$

with

$$\Omega = \operatorname{sgn}(w)\, F_c - F\,, \tag{13}$$

when the velocity sign changes. The average stiffness capacity Ω of interacting asperities memorizes the last motion reversal, at which the asperity junctions are released and reloaded again in the opposite direction. The integrated relative displacement q_r is reset to zero whenever the motion direction changes. Solely two parameters, the Coulomb friction F_c and the initial stiffness K, determine the overall hysteresis map of the pre-sliding friction.
The transient friction state

$$\dot{z}_2 = \frac{S(w) - F}{|S(w)|}\,, \tag{14}$$

behaves as a first-order time delay element that transfers the velocity-dependent dynamic friction and attracts it towards the steady-state $S(w) = s(w) + \sigma\, w$. The factor σ constitutes the linear viscous friction term and the nonlinear characteristic curve

$$s(w) = \operatorname{sgn}(w)\Big(F_c + (F_s - F_c)\exp\big(-|\frac{w}{V_s}|^{\delta}\big)\Big) \tag{15}$$

describes the well-known Stribeck effect. The velocity-dependent Stribeck map is upper bounded by the static friction (also called stiction) force F_s and low bounded by the Coulomb friction force. The exponential factors V_s and δ denote the Stribeck velocity and the Stribeck shape factor correspondingly. In Eq. (11), the attraction gain B determines how fast the overall friction force converges towards the steady-state. The attraction gain is additionally subject to the velocity magnitude. On the one hand, this is done in order to reduce the impact of the transient behavior in vicinity to zero velocity, at which the pre-sliding frictional mechanisms predominate. On the other hand, the velocity-dependent attraction gain ensures the steady-state convergence as $|w|$ increases.

Overall seven free parameters are required to describe the dynamic friction using 2SEP model, where five of them are already spent to support the standard Stribeck effect. Here, it is important to say that other dynamic friction models which capture the basic frictional phenomena can be applied in equal manner when describing the overall joint behavior. At this, the most significant aspects by the choice of a particular friction model are the ease of implementation, generality, as well as practicability in terms of the identification to be done under the circumstances of a real operation mode.

3.3 Nonlinear stiffness with hysteresis

In the simplest case the robot joint stiffness can be represented by a linear function of the relative angular displacement across the joint transmission. This somehow archaic but still widely used and, in particular, robust approach relates the joint torque transmission to a classical spring behavior. Nevertheless, most compliant mechanical structures are well known to exhibit a kind of the hardening properties. That is an increasing relative displacement or better to say deflection of the transmitting elements causes an increase of the overall joint stiffness, and thus leads to higher torque rates. Hence, the joint stiffness which is the inverse compliance of all embedded transmitting elements appears as variable, depending on the ongoing joint load. In order to account for variable stiffness properties several manufacturers of gears and components as well as some works published by researchers suggest to use a piecewise linear stiffness approximation with multiple characteristical segments. An alternative to describe the variable stiffness characteristics is to use the polynomial functions whose coefficients have to be fitted from the accurate laboratory measurements.

Since a nonlinear transmission spring is coupled with corresponding hysteresis effects as mentioned in Section 2.2 a suitable hysteresis map has to be also incorporated. A huge number of available hysteresis approaches (see e.g. Bertotti & Mayergoyz (2006)), originated from different domains of natural and technical science, allow a certain freedom by choosing an appropriate model. The well established Bouc-Wen (Bouc (1967), Wen (1976)) hysteresis model as well as its numerous differential extensions (see survey provided by Ismail et al. (2009)) appears to be particulary suitable for those purposes. The Bouc-Wen hysteresis model, which originated from the structural mechanics, uses a first-order non-linear differential equation that relates the relative displacement to the restoring force in a hysteretic way. At this, the shape of the displacement-force hysteresis is controlled by a compact set of free parameters to be determined in each particular case. Another advantage of a Bouc-Wen-like hysteresis modeling is the possibility to incorporate more complex nonlinear stiffness characteristics, as suggested by Ruderman et al. (2010) and shown in the following in more detail.

The restoring torque arising in a hysteretic spring is subdivided into an elastic and plastic (irreversible) part related to each other by a weighting factor. When using the polynomials $k_1, \ldots, k_i$ for describing the characteristic stiffness curve the total restoring torque can be expressed as a superposition

$$\Gamma(\delta,\, x) = \sum_i \left(\mu\, k_i\, \mathrm{sgn}(\delta)\, |\delta|^i + (1-\mu)\, k_i\, \mathrm{sgn}(x)\, |x|^i\right). \tag{16}$$

At this, the weighting coefficient $0 < \mu < 1$ provides a relationship between the purely elastic ($\mu = 1$) and purely hysteretic, further also as plastic, ($\mu = 0$) deflection. The dynamic state variable x which captures the elasto-plastic deflection, therefore responsible for arising hysteresis, is described by

$$\dot{x} = A\,\dot{\delta} - \beta\,|\dot{\delta}|\,|x|^{n-1}x - \gamma\,\dot{\delta}\,|x|^n\,. \tag{17}$$

The amplitude and shape of hysteresis are determined by the parameters A, β, and γ. The factor $n \geq 1$ provides the smoothness of transition between an elastic and plastic response. For an interested reader a more extensive parameter analysis of Bouc-Wen-like differential

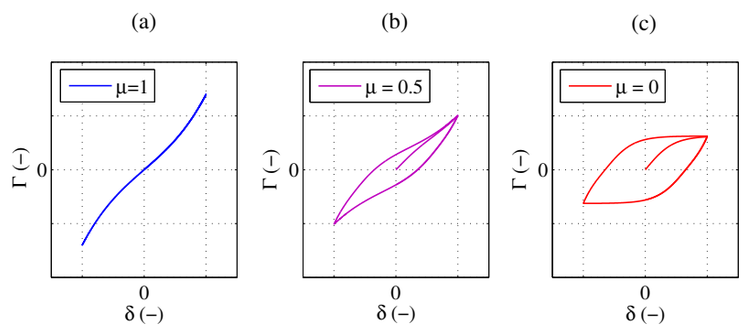

Fig. 9. Hysteretic restoring torque for purely elastic (a), elasto-plastic (b), and plastic (c) torsional deflection

hysteresis models can be found by Ma et al. (2004). In Fig. 9, an example of the restoring torque on a closed load-release cycle is shown dependent on the factor μ. At this, the residual model parameters have been held by the same values. It is evident that no hysteresis losses occur for μ=1, and the case represented in Fig. 9 (a) provides a simple nonlinear characteristic stiffness curve with hardening properties. Though the larger a plastic contribution to the overall restoring torque is the larger is the hysteresis area in Fig. 9 (b) and (c), and the larger is the corresponding structural damping acting in the joint transmission.
With respect to the joint structure derived in Section 3.1 the overall transmitted joint torque is given by

$$T = \Gamma(\delta) + D\,\dot{\delta}\,. \tag{18}$$

Note that the transmitted joint torque already includes the nominal gear ratio N captured by δ. When replacing the nonlinear function $\Gamma(\cdot)$ by a linear spring described by $K\delta$ a simple joint transmission model with linear stiffness and damping can be achieved again. However, when accounting for hysteresis motion losses the use of a hysteresis stiffness map becomes indispensable and has to be included in the overall joint dynamics.

4. Experimental case study

In the following, let us analyze the experimental observations together with some exemplary identification results obtained on the laboratory setup of an elastic revolute joint. The deployed laboratory setup depicted in Fig. 10 has been designed and constructed at the Institute of Control Theory and Systems Engineering of Technical University Dortmund and is primarily intended for investigating the single joint behavior as well as for the control experiments. The testbed contains a standard BLDC motor with rated power 400 W and idling speed 3100 rpm. The servo drive is equipped by a 15-bit resolver and is energized by a PWM electronic unit with onboard current control loop of 11 kHz rate. Through a torsionally stiff

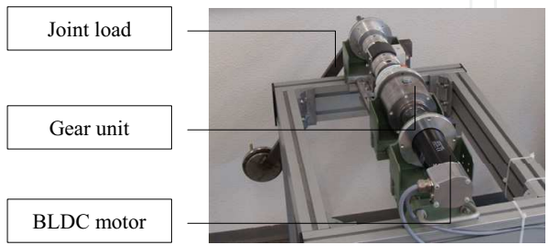

Fig. 10. Laboratory setup of elastic revolute joint

compensating coupling the servo drive is connected to the lightweight harmonic drive gear set (160:1) embedded in a rigid casting. On the output of gear transmission a high-precise absolute encoder with 20-bit resolution is mounted. Using the fixture with couplings a contactless torque cell is applied to measure the output torque for both bounded and free joint motion. Behind the torque measurement the output shaft is equipped with a mechanical interface in order to attach the link rod with adjustable additional weights. Note that the torsional deflection is determined as a difference between the output joint angle and input joint angle captured on the motor shaft.

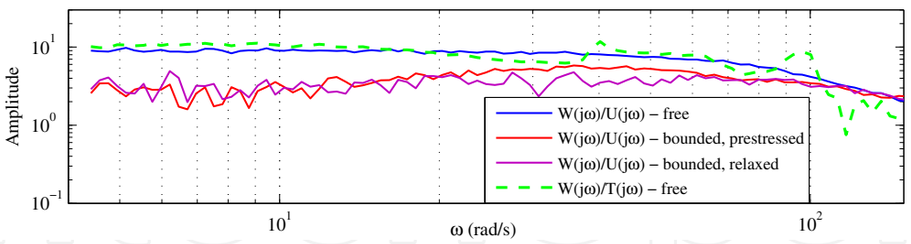

Fig. 11. Frequency response functions measured at different excitation conditions

Before looking on the identification results let us analyze first the obtained frequency response functions (FRF)s of the joint actuator. Four FRFs depicted in Fig. 11 are measured at the different excitation conditions. The transfer from the input torque $U(j\omega)$ to the angular velocity $W(j\omega)$ is realized once for a free and once for a bounded motion for which the output joint shaft was locked. As a controlled input excitation the short impulse of 5 A amplitude and 1.5 ms duration is applied. The bounded motion response is obtained once for a relaxed and once for a prestressed joint state. The latter one means that before applying the input impulse the motor shaft was turned manually in the same motion direction until the elastic transmission becomes fully twisted but does not rotate back due to the friction. The bounded

prestressed FRF exhibits a slight resonance increase due to the raised joint elasticity comparing to the bounded relaxed and the free FRF. At the same time, the high structural and frictional damping impedes the occurrence of significant resonances which could be related to the joint elasticities. The transfer from the joint torque $T(j\omega)$ to the angular velocity $W(j\omega)$ illustrates a backward propagation of reactive restoring torque coming from the joint load. The torque excitation is realized by an external shock applied mechanically to the load part of the joint. The $W(j\omega)/T(j\omega)$ FRF coincides qualitatively with the $W(j\omega)/U(j\omega)$ FRF of free motion despite a high level of process and measurement noise.

Further, let us examine the identification of the joint actuator including the nonlinear friction and the total inertia of the motor and gear assembly. Using the available motor current and joint torque as the inputs and the angular actuator velocity as the output the identification problem can be easily solved in the least-squares sense. The system is excited by a down-chirp signal with 30–1 Hz frequency range. The measured and identified velocity response shown in Fig. 12 exhibits some resonant and anti-resonant phases related to the overall system dynamics.

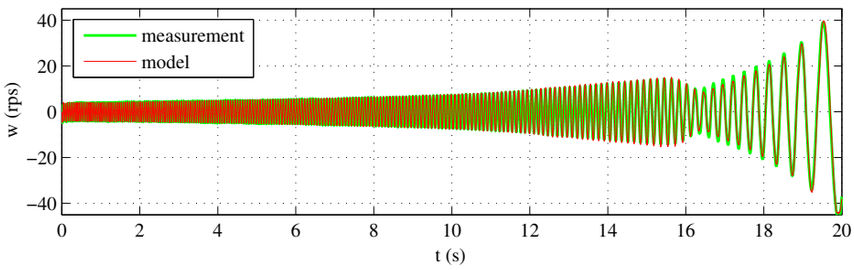

Fig. 12. Measured and identified velocity response to the down-chirp excitation

In the similar manner, the nonlinear joint transmission can be identified using the joint torque and torsion measurements obtained from the same experiment. The time series of the measured and identified joint torque is depicted in Fig. 13 (a). It is easy to recognize that both curves coincide fairly well with each other, thus proving the transmission model to be capable of describing the dynamic joint behavior. Note that the visible discrepancies occur rather at low frequencies at $t > 19$ s. Here, the joint output vibrations which come from the non-smoothly moving load part influence the torque and angular measurements in a non-congruent way. The corresponding torsion-torque hysteresis depicted in Fig. 13 (b) confirms ditto a good agreement between the measured and modeled response, and that for a large set of the nested hysteresis loops.

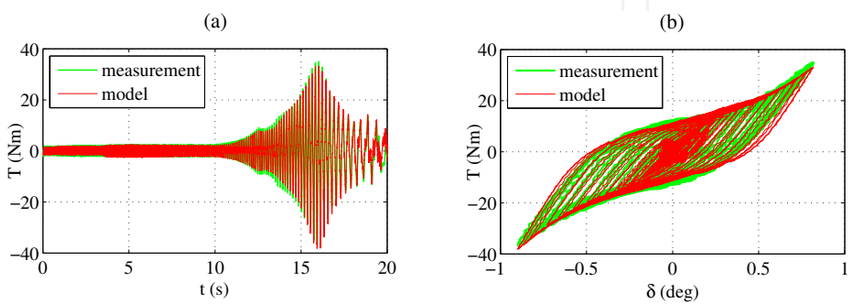

Fig. 13. Measured and identified joint torque, (a) time series, (b) torsion-torque hysteresis

Finally, the diagrams provided in Fig. 14 visualize some identification results related to the joint load. The gravity term can be determined in a quite simple way using the quasi-static motion experiments. The joint link is driven slowly across the overall operation space by using the lowest possible constant input torque. The obtained measurements of the joint torque and output angular position are used to fit the gravity as shown in Fig. 14 (a). The measured and predicted velocity response of the identified joint load is shown in Fig. 14 (b) for the applied step excitation. The peak velocity of about 60 deg/s is in the upper operation range of the experimental joint setup. A substantial velocity decrease occurs due to an increasing impact of gravity. Note that the depicted (measured) joint torque constitutes the total torque balance behind the gear affected simultaneously by the transmitted actuator torque and reactive torque of the joint load. A clearly visible oscillation pattern indicates the impact of the output joint shaft and link vibrations.

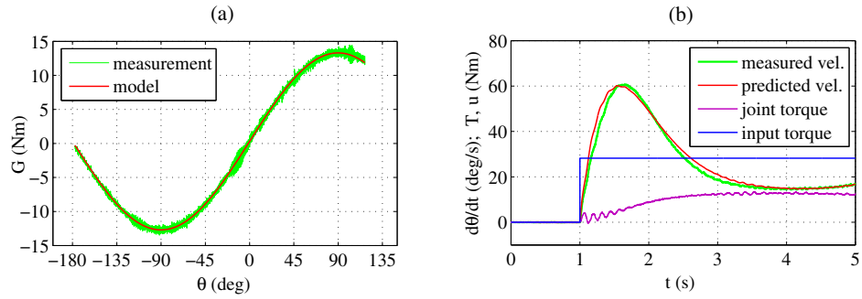

Fig. 14. Measured and identified gravity torque (a), measured and predicted velocity response of the joint load together with the measured applied and transmitted torque (b)

5. Conclusions

The presented methodology aims for analyzing and modeling the behavior of elastic robot joints with nonlinearities such as hysteresis and friction which affect the stiffness and damping characteristics. Independent of the rigid or elastic joint consideration a general topology of revolute robot joints has been demonstrated as a starting position for a subsequent, more detailed system modeling. The defined forward and feedback paths allow to decompose the robot joint into the close physical subsystems with appropriate eigenbehavior. This permits to cut free the entire joint, and to analyze and identify its subsystems stand-alone, under the terms of fully or partially measurable states. For a large class of rotary joint transmissions a sophisticated but nevertheless manageable model has been proposed. In addition to numerical examples an experimental case study has been shown to prove the proposed methods.

6. References

Al-Bender, F. & Swevers, J. (2008). Characterization of friction force dynamics, *IEEE Control Systems Magazine* 28(6): 64–81.

Albu-Schaffer, A., Eiberger, O., Grebenstein, M., Haddadin, S., Ott, C., Wimbock, T., Wolf, S. & Hirzinger, G. (2008). Soft robotics, *IEEE Robotics Automation Magazine* 15(3): 20–30.

Armstrong-Helouvry, B. & Chen, Q. (2008). The Z-properties chart, *IEEE Control Systems Magazine* 28(5): 79–89.

Armstrong-Helouvry, B., Dupont, P. & de Wit, C. C. (1994). A survey of modeling, analysis tools and compensation methods for the control of machines with friction, *Automatica* 30: 1083–1138.

Bertotti, G. & Mayergoyz, I. D. (2006). *The Science of Hysteresis 1–3*, first edn, Academic Press.

Bona, B. & Indri, M. (2005). Friction compensation in robotics: an overview, *Proc. 44th IEEE Conference on Decision and Control, and the European Control Conferenc*, Seville, Spain, pp. 4360–4367.

Bouc, R. (1967). Forced vibration of mechanical systems with hysteresis, *Proc. 4th Conference on Nonlinear Oscillations*, Prague, Czechoslovakia.

De Wit, C. C. & Praly, L. (2000). Adaptive eccentricity compensation, *IEEE Transactions on Control Systems Technology* 8(5): 757–766.

Dhaouadi, R., Ghorbel, F. H. & Gandhi, P. S. (2003). A new dynamic model of hysteresis in harmonic drives, *IEEE Transactions on Industrial Electronics* 50(6): 1165–1171.

Ferretti, G., Magnani, G. & Rocco, P. (2004). Impedance control for elastic joints industrial manipulators, *IEEE Transactions on Robotics and Automation* 20(3): 488–498.

Ismail, M., Ikhouane, F. & Rodellar, J. (2009). The hysteresis Bouc-Wen model, a survey, *Archives of Computational Methods in Engineering* 16(2): 161–188.

Ma, F., Zhang, H., Bockstedte, A., Foliente, G. C. & Paevere, P. (2004). Parameter analysis of the differential model of hysteresis, *ASME Journal of Applied Mechanics* 71(3): 342–349.

Ott, C., Albu-Schaeffer, A., Kugi, A. & Hirzinger, G. (2008). On the passivity-based impedance control of flexible joint robots, *IEEE Transactions on Robotics* 24(2): 416–429.

Ruderman, M. & Bertram, T. (2010). Friction model with elasto-plasticity for advanced control applications, *Proc. IEEE/ASME International Conference on Advanced Intelligent Mechatronics (AIM2010)*, Montreal, Canada, pp. 914–919.

Ruderman, M. & Bertram, T. (2011a). FRF based identification of dynamic friction using two-state friction model with elasto-plasticity, *Proc. IEEE International Conference on Mechatronics (ICM 2011)*, Istanbul, Turkey, pp. 230–235.

Ruderman, M. & Bertram, T. (2011b). Modified Maxwell-slip model of presliding friction, *Proc. 18th IFAC World Congress*, Milan, Italy, pp. 10764–10769.

Ruderman, M., Bertram, T. & Aranovskiy, S. (2010). Nonlinear dynamic of actuators with elasticities and friction, *Proc. IFAC 5th Symposium on Mechatronic Systems*, MA, USA, pp. 255–260.

Ruderman, M., Hoffmann, F. & Bertram, T. (2009). Modeling and identification of elastic robot joints with hysteresis and backlash, *IEEE Transactions on Industrial Electronics* 56(10): 3840–3847.

Sciavicco, L. & Siciliano, B. (2000). *Modelling and Control of Robot Manipulators*, second edn, Springer, Berlin, Germany.

Spong, M. W. (1987). Modeling and control of elastic joint robots, *Journal of Dynamic Systems, Measurement, and Control* 109(4): 310–319.

Taghirad, H. D. & Bélanger, P. R. (1998). Modeling and parameter identification of harmonic drive systems, *Journal of Dynamic Systems, Measurement, and Control* 120(4): 439–444.

Thummel, M., Otter, M. & Bals, J. (2005). Vibration control of elastic joint robots by inverse dynamics models, *Solid Mechanics and its Applications* 130: 343–354.

Tjahjowidodo, T., Al-Bender, F. & Brussel, H. V. (2006). Nonlinear modelling and identification of torsional behaviour in Harmonic Drives, *Proc. International Conference on Noise and Vibration Engineering (ISMA2006)*, Leuven, Belgium, pp. 2785–2796.

Wen, Y. K. (1976). Method for random vibration of hysteretic systems, *ASCE Journal of the Engineering Mechanics Division* 102(2): 249–263.

Zollo, L., Siciliano, B., Luca, A. D., Guglielmelli, E. & Dario, P. (2005). Compliance control for an anthropomorphic robot with elastic joints: Theory and experiments, *Journal of Dynamic Systems, Measurement, and Control* 127(3): 321–328.

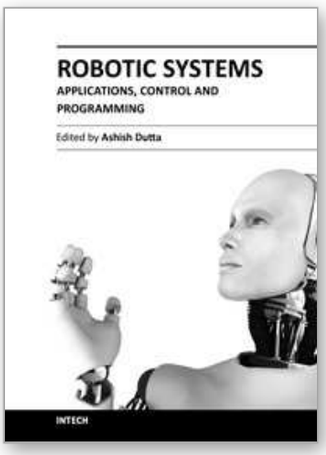

Robotic Systems - Applications, Control and Programming
Edited by Dr. Ashish Dutta

ISBN 978-953-307-941-7
Hard cover, 628 pages
Publisher InTech
Published online 03, February, 2012
Published in print edition February, 2012

This book brings together some of the latest research in robot applications, control, modeling, sensors and algorithms. Consisting of three main sections, the first section of the book has a focus on robotic surgery, rehabilitation, self-assembly, while the second section offers an insight into the area of control with discussions on exoskeleton control and robot learning among others. The third section is on vision and ultrasonic sensors which is followed by a series of chapters which include a focus on the programming of intelligent service robots and systems adaptations.

InTech Europe
University Campus STeP Ri
Slavka Krautzeka 83/A
51000 Rijeka, Croatia
Phone: +385 (51) 770 447
Fax: +385 (51) 686 166
www.intechopen.com

InTech China
Unit 405, Office Block, Hotel Equatorial Shanghai
No.65, Yan An Road (West), Shanghai, 200040, China
中国上海市延安西路65号上海国际贵都大饭店办公楼405单元
Phone: +86-21-62489820
Fax: +86-21-62489821

IntechOpen